



The MITC3+ shell element and its performance



Youngyu Lee^a, Phill-Seung Lee^{a,*}, Klaus-Jürgen Bathe^b

^a Division of Ocean Systems Engineering, Korea Advanced Institute of Science and Technology, 291 Daehak-ro, Yuseong-gu, Daejeon 305-701, Republic of Korea

^b Department of Mechanical Engineering, Massachusetts Institute of Technology, Cambridge, MA 02139, USA

ARTICLE INFO

Article history:

Received 2 January 2014

Accepted 22 February 2014

Keywords:

Shell structures
Shell finite elements
3-Node element
MITC method
Convergence

ABSTRACT

In this paper, we present an effective new 3-node triangular shell finite element, called the MITC3+ element. The new shell element is based on the concepts earlier published for the MITC3 shell element (Lee and Bathe, 2004) [1] but is enriched by a cubic bubble function for the rotations. A new assumed transverse shear strain field is developed for the element. The shell element passes the three basic tests (the isotropy, patch and zero energy mode tests) and shows excellent convergence behavior in basic and encompassing convergence tests.

© 2014 Elsevier Ltd. All rights reserved.

1. Introduction

During the last decades, the finite element method has been widely used for the analysis of shell structures. However, although a great effort has been expended to develop an effective 3-node shell finite element, no element is currently available that has been shown to be reliable and effective in the analysis of general shell structures [1–11]. Such element should show isotropic behavior and pass the consistency, ellipticity and inf-sup conditions and hence be optimal in convergence regardless of the shell geometry, thickness of the shell, boundary conditions and applied loading [2,3]. The highly sensitive and complex behavior of shell structures has made it extremely difficult to establish such an element [3,12–16].

Shell structures can exhibit membrane dominated, bending dominated and mixed behaviors, with high strain gradients in internal and boundary layers. An effective finite element formulation should be able to represent these behaviors and converge at optimal rate in an appropriate norm for any shell thickness. If a finite element discretization cannot accurately approximate the pure bending displacement fields of shells, the solution accuracy deteriorates in bending dominated and mixed shell behaviors. This phenomenon is called “locking” and can be severe when the shell thickness decreases [2,3,12]. To alleviate the locking behavior, while preserving the properties of consistency and ellipticity, the MITC method has been successfully used to establish quadrilateral and triangular shell elements [1,2,17–21]. However, while the

3-node triangular MITC3 element is useful, the element is not optimal in its convergence behaviors [1,11].

An important point is that to generate meshes for a triangular shell element is relatively easy, even for complex shell analyses. In addition, an effective 3-node shell element would be attractive due to the small bandwidth of the governing global stiffness and mass matrices. So far, 4-node quadrilateral shell elements, and notably the 4-node MITC4 element, have been dominantly used in practice due to their superior performance compared to triangular shell elements. However, these quadrilateral elements deteriorate in their convergence behaviors when the elements are geometrically distorted, see e.g. Ref. [22].

In general, 3-node triangular elements for the two-dimensional analysis of solids and the analysis of shells suffer from a lack of displacement modes [2,9,10]. To overcome this inherent limitation in some elements, a scheme to enrich the displacement field can be effective [22–25]. In particular, bubble functions have been used to improve the predictive capability of finite elements for two- and three-dimensional solid and fluid flow analyses, and for plate and shell solutions [2,20,24,26–29]. A cubic bubble function for a 3-node triangular element is attractive [24,26] because it provides a higher-order interpolation inside the element while maintaining the linear interpolation along the element edges, thus providing compatibility between elements.

In the development of the new triangular 3-node shell element, which we call the MITC3+ shell element, we use a cubic bubble function for the interpolation of the rotations to enrich the bending displacements. That is, **only 2 internal rotation degrees of freedom are added to the standard 3-node shell element**. Hence, the bubble function does not affect the mid-surface displacement of the shell

* Corresponding author. Tel.: +82 42 350 1512; fax: +82 42 350 1510.

E-mail address: phillseung@kaist.edu (P. S. Lee).

element, and the corresponding degrees of freedom can be statically condensed out on the element level.

To reduce shear locking in the shell element, a new assumed transverse shear strain field is designed. The MITC3+ shell element passes all basic tests, that is, the isotropy, zero energy mode and patch tests, and shows an excellent convergence behavior in the solution of plate and shell benchmark problems, even when severely distorted meshes are used.

In the following sections, the formulation of the MITC3+ shell element is given and the performance of the element is presented.

2. Formulations of the triangular shell finite elements

In this section, we briefly recall the formulation of the MITC3 shell element and then present the formulation of the new MITC3+ shell element.

2.1. The MITC3 shell finite element

The geometry of a standard 3-node continuum mechanics based triangular shell finite element is interpolated using [1,2]

$$\vec{x}(r, s, t) = \sum_{i=1}^3 h_i(r, s) \vec{x}_i + \frac{t}{2} \sum_{i=1}^3 a_i h_i(r, s) \vec{V}_n^i \quad \text{with} \quad (1)$$

$$h_1 = 1 - r - s, \quad h_2 = r, \quad h_3 = s,$$

where $h_i(r, s)$ is the two-dimensional interpolation function of the standard isoparametric procedure corresponding to node i , \vec{x}_i is the position vector of node i in the global Cartesian coordinate system, and a_i and \vec{V}_n^i denote the shell thickness and the director vector at the node, see Fig. 1.

The corresponding displacement interpolation of the element is

$$\vec{u}(r, s, t) = \sum_{i=1}^3 h_i(r, s) \vec{u}_i + \frac{t}{2} \sum_{i=1}^3 a_i h_i(r, s) (-\vec{V}_2^i \alpha_i + \vec{V}_1^i \beta_i), \quad (2)$$

in which \vec{u}_i is the nodal displacement vector in the global Cartesian coordinate system, \vec{V}_1^i and \vec{V}_2^i are unit vectors orthogonal to \vec{V}_n^i and to each other, and α_i and β_i are the rotations of the director vector \vec{V}_n^i about \vec{V}_1^i and \vec{V}_2^i , respectively, at node i .

The linear terms of the displacement-based covariant strain components are given by

$$e_{ij} = \frac{1}{2} (\vec{g}_i \cdot \vec{u}_j + \vec{g}_j \cdot \vec{u}_i), \quad (3)$$

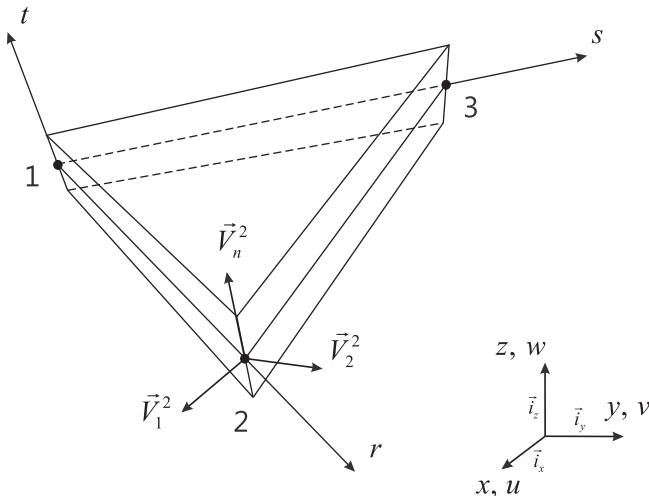


Fig. 1. A standard 3-node triangular continuum mechanics based shell finite element.

in which

$$\vec{g}_i = \frac{\partial \vec{x}}{\partial r_i}, \quad \vec{u}_i = \frac{\partial \vec{u}}{\partial r_i} \quad \text{with} \quad r_1 = r, r_2 = s, r_3 = t. \quad (4)$$

Since the 3-node triangular shell finite element is flat, the covariant in-plane strain components are calculated using Eqs. (1)–(3). However, the covariant transverse shear strain field is established using the MITC scheme. The transverse shear strain field of the MITC3 shell element is based on assuming constant covariant transverse shear strain conditions along the edges

$$\tilde{e}_{rt}^{\text{MITC3}} = e_{rt}^{(1)} + cs, \quad \tilde{e}_{st}^{\text{MITC3}} = e_{st}^{(2)} - cr, \quad (5)$$

where $c = (e_{rt}^{(3)} - e_{rt}^{(1)}) - (e_{st}^{(3)} - e_{st}^{(2)})$ and the tying points are shown in Fig. 2 [1].

2.2. The MITC3+ shell finite element

The geometry interpolation of the MITC3+ shell element, shown in Fig. 3, is given by

$$\vec{x}(r, s, t) = \sum_{i=1}^3 h_i(r, s) \vec{x}_i + \frac{t}{2} \sum_{i=1}^4 a_i f_i(r, s) \vec{V}_n^i \quad \text{with} \quad (6)$$

$$a_4 \vec{V}_n^4 = \frac{1}{3} (a_1 \vec{V}_n^1 + a_2 \vec{V}_n^2 + a_3 \vec{V}_n^3),$$

in which the $f_i(r, s)$ are two-dimensional interpolation functions that include the cubic bubble function f_4 corresponding to the internal node 4

$$f_1 = h_1 - \frac{1}{3}f_4, \quad f_2 = h_2 - \frac{1}{3}f_4, \quad f_3 = h_3 - \frac{1}{3}f_4, \quad f_4 = 27rs(1-r-s). \quad (7)$$

From Eq. (6), we obtain the displacement interpolation [1]

$$\vec{u}(r, s, t) = \sum_{i=1}^3 h_i(r, s) \vec{u}_i + \frac{t}{2} \sum_{i=1}^4 a_i f_i(r, s) (-\vec{V}_2^i \alpha_i + \vec{V}_1^i \beta_i), \quad (8)$$

in which α_4 and β_4 are the rotation degrees of freedom at the bubble node.

The bubble node, with rotation degrees of freedom only, is positioned on the flat surface defined by the three corner nodes of the element. Only the bending and transverse shear strain fields are enriched by the bubble function, and the geometry of the element would remain flat, as for the MITC3 element, if a large deformation analysis were pursued. Also, static condensation can be carried out on the element level for the rotations α_4 and β_4 .

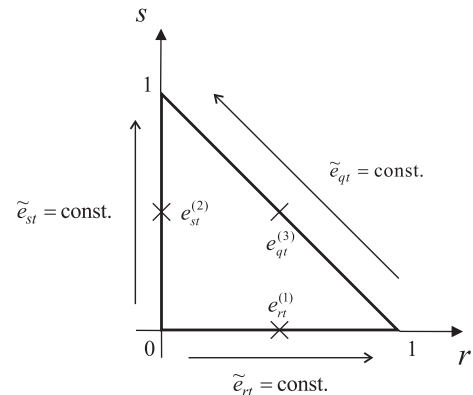


Fig. 2. Tying positions for the assumed transverse shear strain field of the MITC3 shell element. The constant transverse shear strain conditions are imposed along its edges.

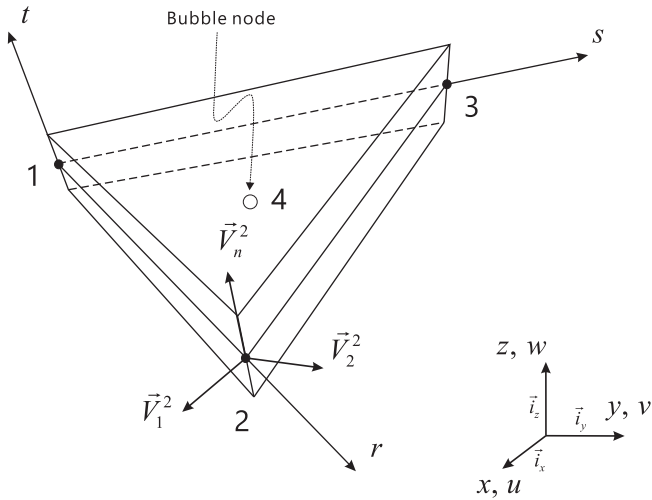


Fig. 3. Geometry of the MITC3+ shell element with an additional bubble node.

As for the MITC3 shell element, we only use the mixed interpolation for the transverse shear strain components, but we must design a new assumed transverse shear strain field because the effect of the bubble function should be included.

To design the new assumed transverse shear strain field, we focus on two considerations. Firstly, the tying points for the covariant transverse shear strain components should be inside the element, that is, not on the element edges as for the MITC3 element, because the bubble function is zero along the element edges. Secondly, the stiffness of the in-plane twisting mode, see Fig. 4, must be reduced [10].

Considering a 3-node triangular shell element (that is, without the node for the bubble), the transverse shear strains occur in two transverse shearing modes and in an in-plane twisting mode. The in-plane twisting mode corresponds to twisting of the element about the axis normal to the mid-surface at the barycenter, $r = s = 1/3$, as shown in Fig. 4, with zero transverse shear strains at that point.

The transverse shear strain field of the MITC3 shell element can be separated into the constant part corresponding to the transverse shearing modes and the linear part corresponding to the in-plane twisting mode.

$$\tilde{e}_{rt}^{MITC3} = \tilde{e}_{rt}^{const.} + \tilde{e}_{rt}^{linear}, \quad \tilde{e}_{st}^{MITC3} = \tilde{e}_{st}^{const.} + \tilde{e}_{st}^{linear}. \quad (9)$$

We can easily obtain the constant part by evaluating the transverse shear strains at the barycenter

$$\begin{aligned} \tilde{e}_{rt}^{const.} &= \tilde{e}_{rt}^{MITC3} \Big|_{s=1/3} = \frac{2}{3} \left(e_{rt}^{(1)} + \frac{1}{2} e_{st}^{(2)} \right) - \frac{1}{3} \left(e_{st}^{(3)} - e_{rt}^{(3)} \right), \\ \tilde{e}_{st}^{const.} &= \tilde{e}_{st}^{MITC3} \Big|_{r=1/3} = \frac{2}{3} \left(e_{st}^{(2)} + \frac{1}{2} e_{rt}^{(1)} \right) + \frac{1}{3} \left(e_{st}^{(3)} - e_{rt}^{(3)} \right). \end{aligned} \quad (10)$$

Subtracting, for the MITC3 shell element, the constant part from the transverse shear strain field in Eq. (5), we obtain the linearly varying part

$$\begin{aligned} \tilde{e}_{rt}^{linear} &= \tilde{e}_{rt}^{MITC3} - \tilde{e}_{rt}^{const.} = \frac{1}{3} c(3s - 1), \\ \tilde{e}_{st}^{linear} &= \tilde{e}_{st}^{MITC3} - \tilde{e}_{st}^{const.} = \frac{1}{3} c(1 - 3r). \end{aligned} \quad (11)$$

If this scheme were used for the new element, the constant part in Eq. (10) would not include the effect of the bubble function since the bubble function is zero along the element edges, that is, at the

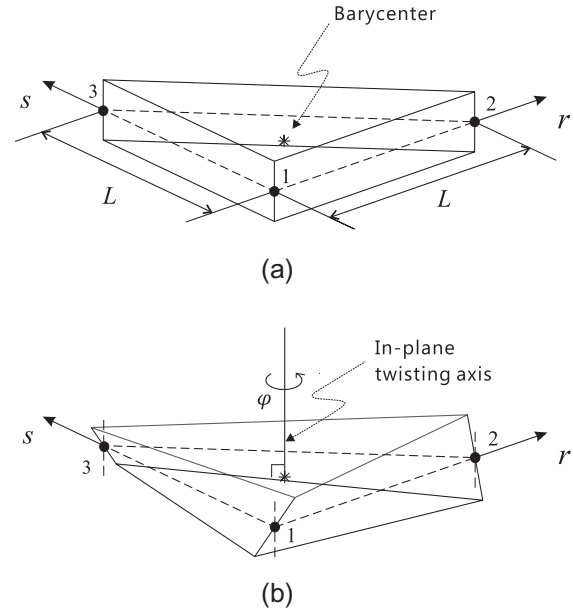


Fig. 4. In-plane twisting mode of a single shell finite element. (a) Undeformed geometry. (b) In-plane twisting mode.

tying positions (1)–(3). To include the effect of the bubble function in the constant part, we design a new tying scheme using element internal points. First, the three covariant transverse shear strains e_{1t} , e_{2t} and e_{3t} are defined in the directions of the internal lines from the barycenter to the corners as shown in Fig. 5(a). The following relations are obtained for the covariant transverse shear strain components, for $0 \leq r, s \leq 1$,

$$e_{1t} = \frac{1}{\sqrt{5}}(2e_{st} - e_{rt}), \quad e_{2t} = \frac{1}{\sqrt{5}}(2e_{rt} - e_{st}), \quad e_{3t} = -\frac{1}{\sqrt{2}}(e_{rt} + e_{st}), \quad (12a)$$

and

$$\begin{aligned} e_{rt} &= \frac{\sqrt{5}}{3} e_{2t} - \frac{\sqrt{2}}{3} e_{3t}, \quad e_{st} = \frac{\sqrt{5}}{3} e_{1t} - \frac{\sqrt{2}}{3} e_{3t}, \\ e_{qt} &= \frac{1}{\sqrt{2}}(e_{st} - e_{rt}) = \frac{\sqrt{10}}{6}(e_{1t} - e_{2t}). \end{aligned} \quad (12b)$$

Using Eq. (12a), the transverse shear strain components are sampled at three internal tying points (A), (B) and (C) on the three internal lines, see Fig. 5(b) and Table 1

$$e_{1t}^{(A)} = \frac{1}{\sqrt{5}}(2e_{st}^{(A)} - e_{rt}^{(A)}), \quad e_{2t}^{(B)} = \frac{1}{\sqrt{5}}(2e_{rt}^{(B)} - e_{st}^{(B)}), \quad e_{3t}^{(C)} = -\frac{1}{\sqrt{2}}(e_{st}^{(C)} + e_{rt}^{(C)}). \quad (13)$$

It is important to note that the tying points have been selected to obtain a spatially isotropic element.

Table 1

Tying positions for the new assumed transverse shear strain fields for the MITC3i and MITC3+ shell elements. The distance d is defined in Fig. 5(c).

	Tying positions	r	s
Fig. 5(b)	(A)	1/6	2/3
	(B)	2/3	1/6
	(C)	1/6	1/6
Fig. 5(c)	(D)	1/3 + d	1/3 - $2d$
	(E)	1/3 - $2d$	1/3 + d
	(F)	1/3 + d	1/3 + d

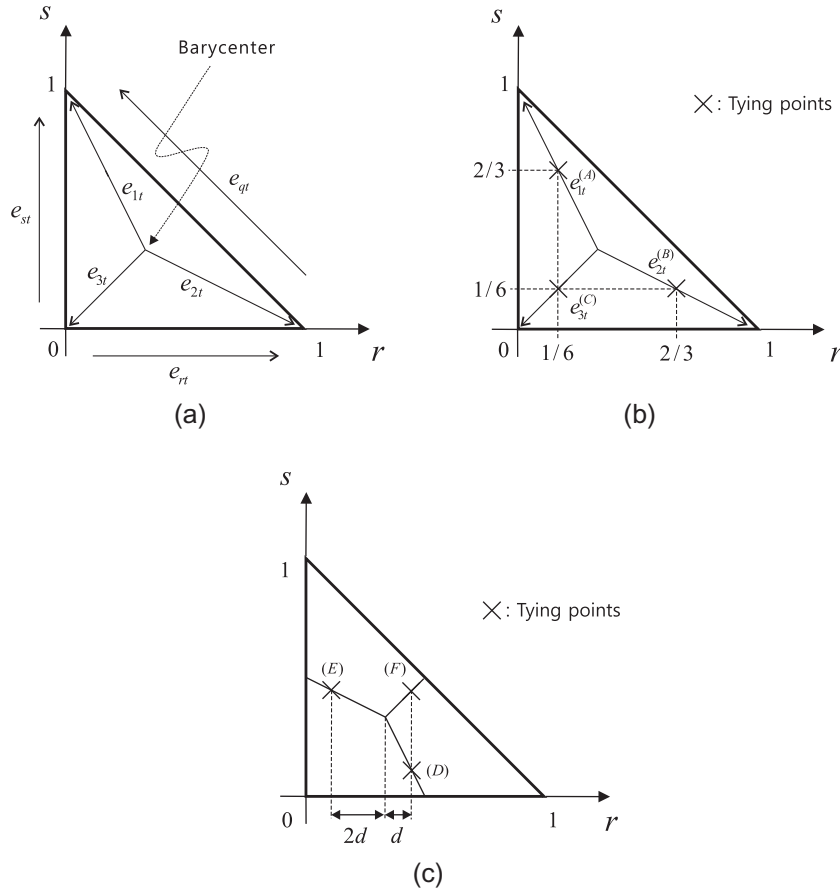


Fig. 5. Transverse shear strains e_{1t} , e_{2t} and e_{3t} , and the tying positions (A)–(F) for the new assumed transverse shear strain field.

Using next the relations in Eq. (12b), the constant covariant transverse shear strains along the element edge directions are assumed to be

$$\begin{aligned} \hat{e}_{rt} &= \frac{\sqrt{5}}{3} e_{2t}^{(B)} - \frac{\sqrt{2}}{3} e_{3t}^{(C)}, & \hat{e}_{st} &= \frac{\sqrt{5}}{3} e_{1t}^{(A)} - \frac{\sqrt{2}}{3} e_{3t}^{(C)}, \\ \hat{e}_{qt} &= \frac{\sqrt{10}}{6} (e_{1t}^{(A)} - e_{2t}^{(B)}), \end{aligned} \quad (14)$$

and, using Eq. (13), a new constant transverse shear strain field is obtained

$$\begin{aligned} \hat{e}_{rt}^{const.} &= \hat{e}_{rt} = \frac{2}{3} \left(e_{rt}^{(B)} - \frac{1}{2} e_{st}^{(B)} \right) + \frac{1}{3} (e_{rt}^{(C)} + e_{st}^{(C)}), \\ \hat{e}_{st}^{const.} &= \hat{e}_{st} = \frac{2}{3} \left(e_{st}^{(A)} - \frac{1}{2} e_{rt}^{(A)} \right) + \frac{1}{3} (e_{rt}^{(C)} + e_{st}^{(C)}). \end{aligned} \quad (15)$$

In order to render the in-plane twisting stiffness more flexible, the linear part is modified by using three new tying points (D), (E) and (F) instead of the tying points (1)–(3) when we evaluate c in Eq. (11)

$$\begin{aligned} \hat{e}_{rt}^{linear} &= \frac{1}{3} \hat{c}(3s-1), & \hat{e}_{st}^{linear} &= \frac{1}{3} \hat{c}(1-3r) \quad \text{with} \\ \hat{c} &= (e_{rt}^{(F)} - e_{rt}^{(D)}) - (e_{st}^{(F)} - e_{st}^{(E)}). \end{aligned} \quad (16)$$

The tying positions (D), (E) and (F) are positioned on the three internal lines from the barycenter to the centers of the edges with d defined in Fig. 5(c) and Table 1. As d varies from $1/6$ to 0 , the three tying positions move from the centers of the edges to the barycenter, resulting in a smaller in-plane twisting stiffness. An effective value for d is determined below.

The new assumed transverse shear strain field is thus given by

$$\begin{aligned} \hat{e}_{rt} &= \hat{e}_{rt}^{const.} + \hat{e}_{rt}^{linear} = \frac{2}{3} \left(e_{rt}^{(B)} - \frac{1}{2} e_{st}^{(B)} \right) + \frac{1}{3} (e_{rt}^{(C)} + e_{st}^{(C)}) + \frac{1}{3} \hat{c}(3s-1), \\ \hat{e}_{st} &= \hat{e}_{st}^{const.} + \hat{e}_{st}^{linear} = \frac{2}{3} \left(e_{st}^{(A)} - \frac{1}{2} e_{rt}^{(A)} \right) + \frac{1}{3} (e_{rt}^{(C)} + e_{st}^{(C)}) + \frac{1}{3} \hat{c}(1-3r). \end{aligned} \quad (17)$$

At this point, it is interesting to consider a 3-node shell finite element in which the geometry and displacement interpolations in Eqs. (1) and (2) and the new assumed transverse shear strain field in Eq. (17) are employed. We label the element as MITC3i and study its performance also in the following sections.

3. Basic numerical tests

In this section, we consider the three basic tests: the isotropy, patch and zero energy mode tests.

The spatially isotropic behavior is an important requirement for triangular shell elements. The element behavior should not depend on the sequence of node numbering, i.e. the element orientation [1]. The numerical procedure for the isotropy element test is given in Refs. [1,10]. The MITC3i and MITC3+ shell elements pass this test.

We perform three patch tests: the membrane, bending and shearing patch tests, see Refs. [1,2] for the patch tests performed. The constant stress fields should be calculated to pass the patch tests. The MITC3i and MITC3+ shell elements pass the three patch tests.

In the zero energy mode test, the number of zero eigenvalues of the stiffness matrix of a single unsupported element are counted

[1,2]. For the MITC3i and MITC3+ shell elements, only the six zero eigenvalues corresponding to the six rigid body modes are obtained when the distance d defined for the tying positions (D), (E) and (F) in Fig. 5(c) is non-zero. As d approaches 0, the eigenvalue corresponding to the in-plane twisting mode in Fig. 4 decreases and is zero when $d = 0$.

A similar phenomenon was investigated for the MITC3-HR shell element in Ref. [10], where it was shown that by decreasing the stiffness for the in-plane twisting mode, it is possible to improve the performance of 3-node shell elements. Therefore, we perform the in-plane twisting mode test given in Ref. [10] and investigate the effect of the distance d .

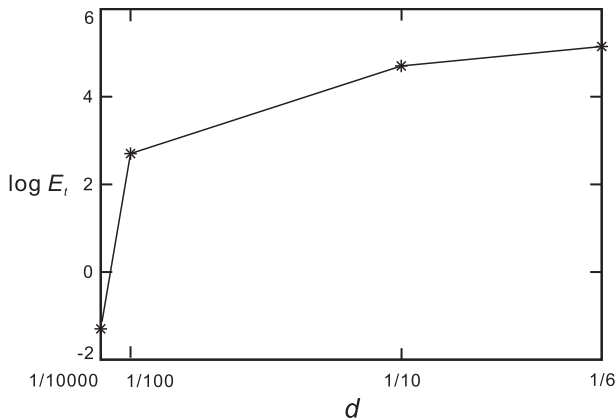


Fig. 6. Strain energy stored in the MITC3i and MITC3+ shell elements depending on the distance d in the in-plane twisting mode. Since the strain energy is proportional to $t \cdot L^2$ in the in-plane twisting mode, E_t is the strain energy normalized by $t \cdot L^2$.

Table 2

Eigenvalues of the stiffness matrix of the single MITC3i shell element for the element geometry shown in Fig. 4(a) when $t/L = 1/10,000$. Note that modes 1 to 6 produce zero eigenvalues corresponding to rigid body modes.

Mode	$d = 1/6$		$d = 1/10$		$d = 1/100$		$d = 1/10,000$	
7	6.6764E-07	B	6.6764E-07	B	6.6764E-07	B	6.6764E-07	B
8	8.1455E-07	B	8.1455E-07	B	8.1454E-07	B	7.9792E-07	B
9	2.4924E-06	B	2.4924E-06	B	2.4924E-06	B	2.4924E-06	B
10	<u>3.6928E+01</u>	T	<u>1.3302E+01</u>	T	<u>1.3306E-01</u>	T	<u>1.3583E-05</u>	T
11	4.6707E+02	S	4.6681E+02	S	4.6667E+02	S	4.6667E+02	S
12	8.3813E+02	M	8.3813E+02	M	8.3813E+02	M	8.3813E+02	M
13	1.1760E+03	S	1.1760E+03	S	1.1760E+03	S	1.1760E+03	S
14	1.3440E+03	M	1.3440E+03	M	1.3440E+03	M	1.3440E+03	M
15	3.0019E+03	M	3.0019E+03	M	3.0019E+03	M	3.0019E+03	M

B: bending modes, T: in-plane twisting mode, S: transverse shearing modes, M: membrane modes.

Table 3

Eigenvalues of the stiffness matrix of the single MITC3+ shell element for the element geometry shown in Fig. 4(a) when $t/L = 1/10,000$. Note that modes 1 to 6 produce zero eigenvalues corresponding to rigid body modes.

Mode	$d = 1/6$		$d = 1/10$		$d = 1/100$		$d = 1/10,000$	
7	6.6685E-07	B	6.6685E-07	B	6.6685E-07	B	6.6685E-07	B
8	8.1273E-07	B	8.1273E-07	B	8.1272E-07	B	7.9621E-07	B
9	2.4921E-06	B	2.4921E-06	B	2.4921E-06	B	2.4921E-06	B
10	8.3211E-06	B+	8.3211E-06	B+	8.3211E-06	B+	8.3107E-06	B+
11	1.4128E-05	B+	1.4128E-05	B+	1.4128E-05	B+	<u>1.3599E-05</u>	T
12	<u>3.6928E+01</u>	T	<u>1.3302E+01</u>	T	<u>1.3306E-01</u>	T	1.4128E-05	B+
13	4.6707E+02	S	4.6681E+02	S	4.6667E+02	S	4.6667E+02	S
14	8.3813E+02	M	8.3813E+02	M	8.3813E+02	M	8.3813E+02	M
15	1.1760E+03	S	1.1760E+03	S	1.1760E+03	S	1.1760E+03	S
16	1.3440E+03	M	1.3440E+03	M	1.3440E+03	M	1.3440E+03	M
17	3.0019E+03	M	3.0019E+03	M	3.0019E+03	M	3.0019E+03	M

B: bending modes, T: in-plane twisting mode, S: transverse shearing modes, M: membrane modes, B+: bending modes due to the bubble function enrichment.

We calculate the strain energies (E_t) of the MITC3i and MITC3+ shell elements when the elements are subjected to the in-plane twisting mode in Fig. 4. We use $L = 1.0$, $E = 1.7472 \times 10^7$ and $\nu = 0.3$. The in-plane twisting mode is given by prescribing the rotations at the nodes to be $\theta_x^1 = \theta_x^3 = \theta_y^1 = \theta_y^2 = 1/\sqrt{12}$ and $\theta_x^2 = \theta_y^3 = -2/\sqrt{12}$. Fig. 6 gives the strain energies of the MITC3i and MITC3+ shell elements as a function of the distance d . When the distance d approaches zero, both shell elements become rapidly more flexible in the in-plane twisting mode.

Tables 2 and 3 present the eigenvalues of the stiffness matrices of the MITC3i and MITC3+ shell elements for the element geometry shown in Fig. 4(a). We consider $t/L = 1/10,000$, $E = 1.7472 \times 10^7$ and $\nu = 0.3$. The eigenvalue corresponding to the in-plane twisting mode decreases as the distance d decreases but is larger than the smallest eigenvalue of a bending mode. Based on this study we choose and always use the distance $d = 1/10,000$. As a consequence, the element formulation contains no spurious zero energy mode, and the ellipticity condition is satisfied. Note that, due to the bubble function enrichment, the MITC3+ shell element contains two additional bending modes compared to the MITC3i shell element.

4. Convergence studies

In this section, we perform convergence studies using appropriate benchmark problems to study the behavior of shell elements: a clamped square plate problem, a sixty-degree skew plate problem, cylindrical shell problems, and hyperboloid shell problems [1–3,30]. These problem solutions pertain to measuring the errors in an appropriate norm considering membrane and bending dominated problems with various shell curvatures, shell thickness values, and boundary conditions.

To measure the error in the finite element solution, we use the s-norm proposed by Hiller and Bathe [31]

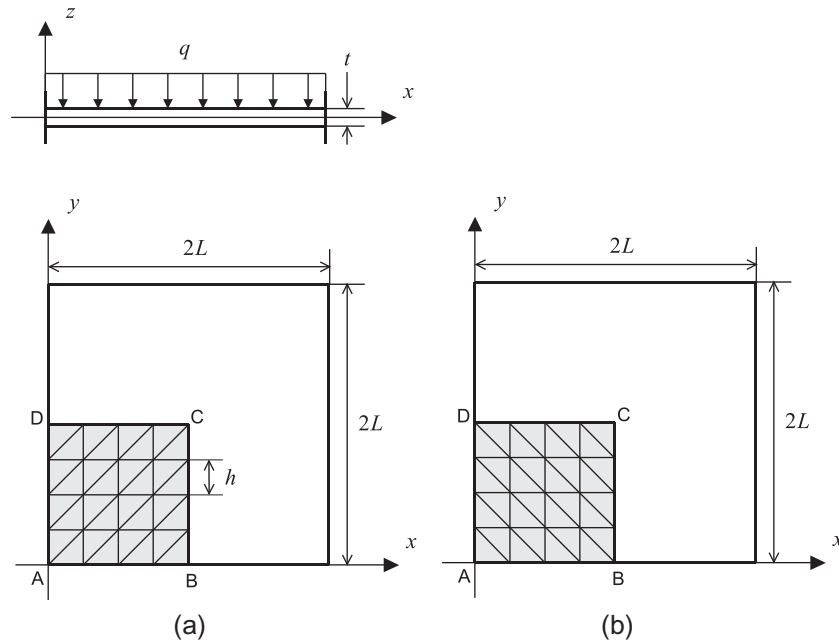


Fig. 7. Fully clamped square plate problem ($L = 1.0$, $E = 1.7472 \times 10^7$, $q = 1.0$ and $\nu = 0.3$) with 2 different 4×4 mesh patterns in (a) and (b).

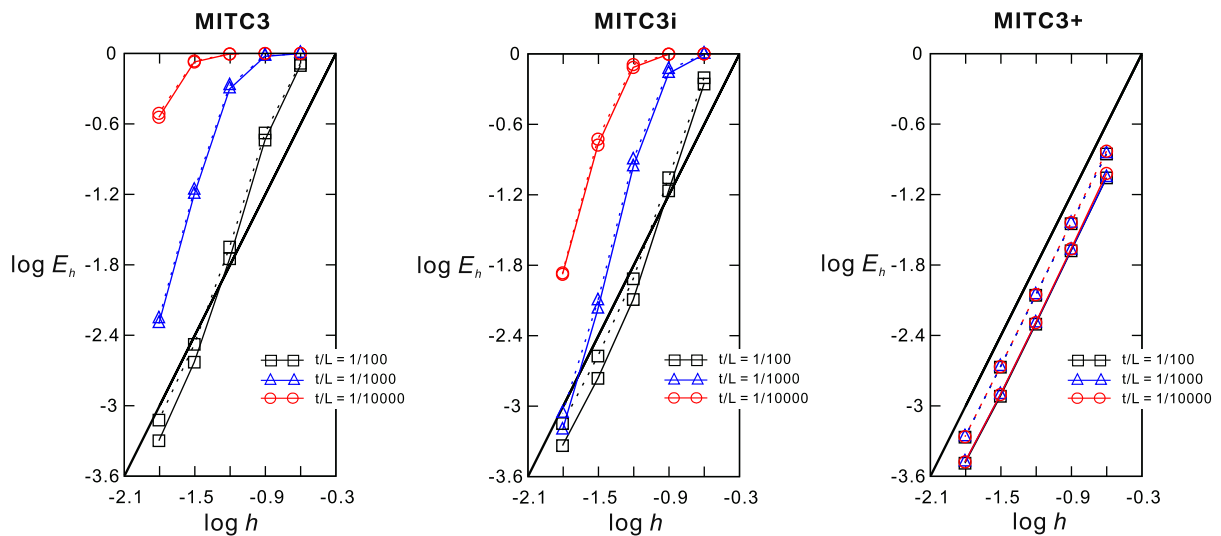


Fig. 8. Convergence curves for the fully clamped square plate problem. The bold line represents the optimal convergence rate. The solid and dotted lines correspond to the results obtained by the mesh patterns in Fig. 7(a) and (b), respectively.

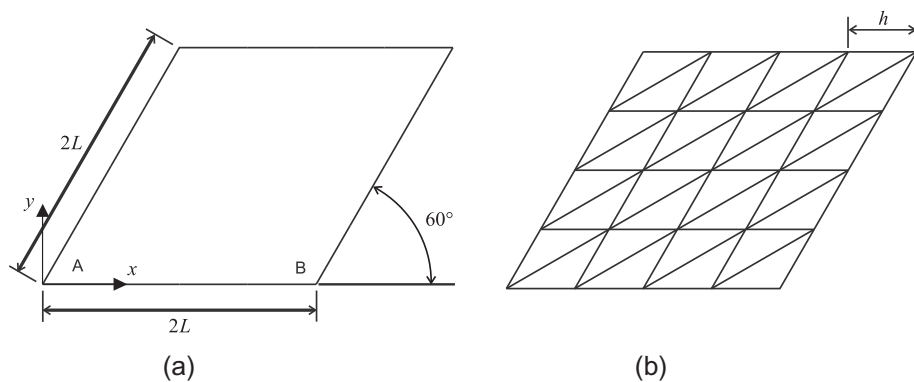


Fig. 9. Simply supported sixty-degree skew plate problem ($L = 1.0$, $E = 1.7472 \times 10^7$ and $\nu = 0.3$). (a) Problem description. (b) Mesh pattern used for $N = 4$.

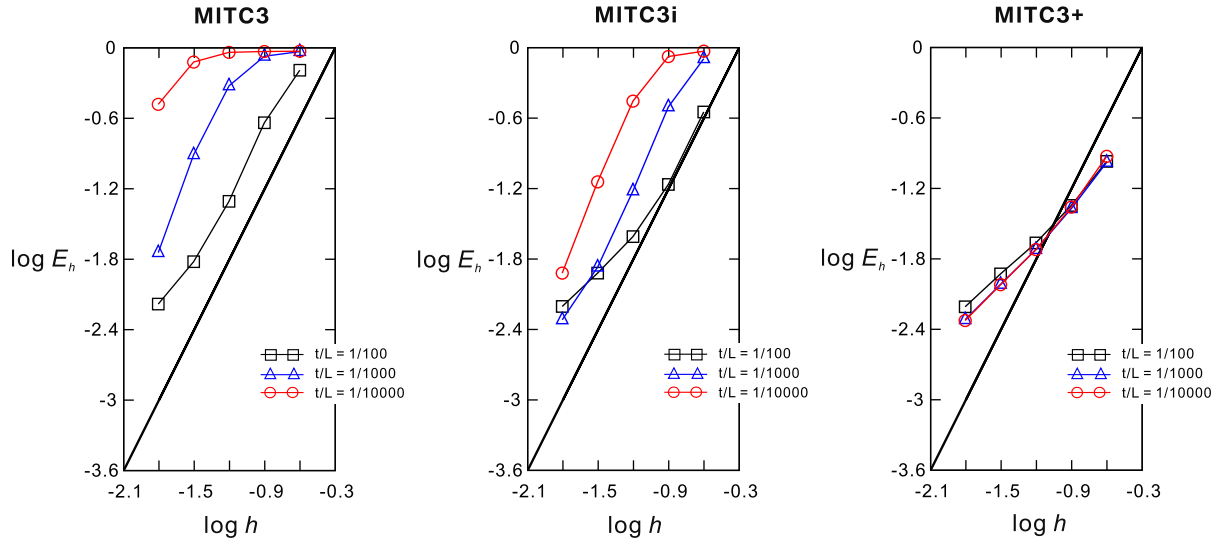


Fig. 10. Convergence curves for the simply supported sixty-degree skew plate problem. The bold line represents the optimal convergence rate.

$$\|\vec{u} - \vec{u}_h\|_s^2 = \int_{\Omega} \Delta \vec{\epsilon}^T \Delta \vec{\tau} d\Omega \quad \text{with} \quad \Delta \vec{\epsilon} = \vec{\epsilon} - \vec{\epsilon}_h,$$

$$\Delta \vec{\tau} = \vec{\tau} - \vec{\tau}_h, \quad (18)$$

where \vec{u} is the exact solution, \vec{u}_h is the solution of the finite element discretization, and $\vec{\epsilon}$ and $\vec{\tau}$ are the strain and stress vectors. The s-norm is suitable to identify whether the finite element formulation satisfies the consistency and inf-sup conditions [3,31–33].

Instead of the exact solution \vec{u} , an accurate finite element solution using a very fine mesh \vec{u}_{ref} can be employed. Then the s-norm in Eq. (18) becomes

$$\|\vec{u}_{ref} - \vec{u}_h\|_s^2 = \int_{\Omega_{ref}} \Delta \vec{\epsilon}^T \Delta \vec{\tau} d\Omega_{ref} \quad \text{with}$$

$$\Delta \vec{\epsilon} = \vec{\epsilon}_{ref} - \vec{\epsilon}_h, \quad \Delta \vec{\tau} = \vec{\tau}_{ref} - \vec{\tau}_h. \quad (19)$$

To measure the performance of finite elements in shell analyses, it is important to consider decreasing shell thickness values. We then use the relative error E_h

$$E_h = \frac{\|\vec{u}_{ref} - \vec{u}_h\|_s^2}{\|\vec{u}_{ref}\|_s^2}. \quad (20)$$

The optimal convergence behavior of the elements, for the shell problems considered, is given by

$$E_h \cong Ch^k, \quad (21)$$

in which h is the element size. For a 3-node shell element to be uniformly optimal, the value of C must be constant, that is, independent of the shell thickness, and $k = 2$.

In this study, well-converged reference solutions calculated using fine meshes of the MITC9 shell elements are used. The MITC9 shell element satisfies the ellipticity and consistency conditions and shows a good convergence behavior [20,30–34].

4.1. Fully clamped square plate problem

We solve the plate bending problem shown in Fig. 7. A square plate of dimensions $2L \times 2L$ and uniform thickness t is subjected to a uniform pressure. All edges are fully clamped (in hard conditions [2]). Due to symmetry, only a one-quarter model is considered, with the following boundary conditions: $u_x = \theta_y = 0$ along BC, $u_y = \theta_x = 0$ along DC and $u_x = u_y = u_z = \theta_x = \theta_y = 0$ along AB and AD.

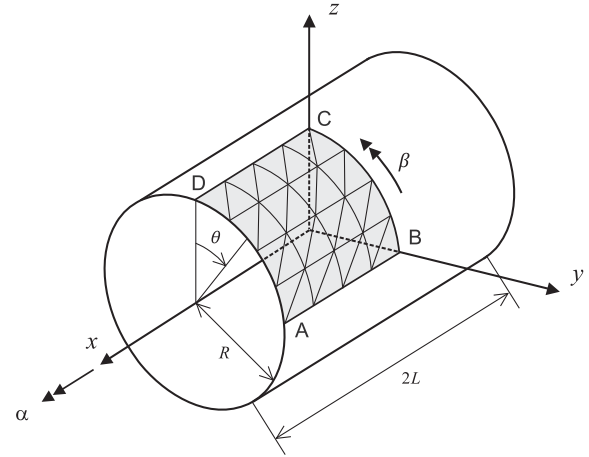


Fig. 11. Cylindrical shell problem (4×4 mesh, $L = R = 1.0$, $E = 2.0 \times 10^5$, $\nu = 1/3$ and $p_0 = 1.0$).

Fig. 8 gives the convergence curves of the MITC3, MITC3i and MITC3+ elements. A 96×96 element mesh of the MITC9 shell element is used to obtain the reference solution. We use $N \times N$ element meshes ($N = 4, 8, 16, 32$, and 64) to calculate the solutions using the triangular shell elements. The element size in the convergence curves is $h = L/N$. The performance of the MITC3+ shell element is best among them and, practically, uniformly optimal. The improved predictive capability of the MITC3i element is observed when compared with the performance of the MITC3 element.

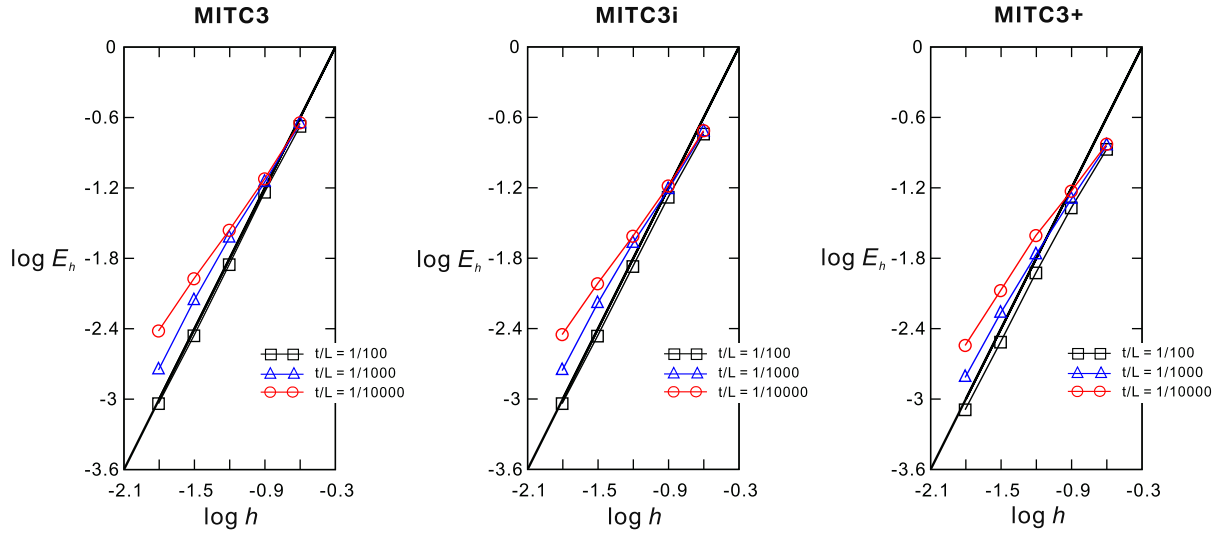


Fig. 12. Convergence curves for the clamped cylindrical shell problem. The bold line represents the optimal convergence rate.

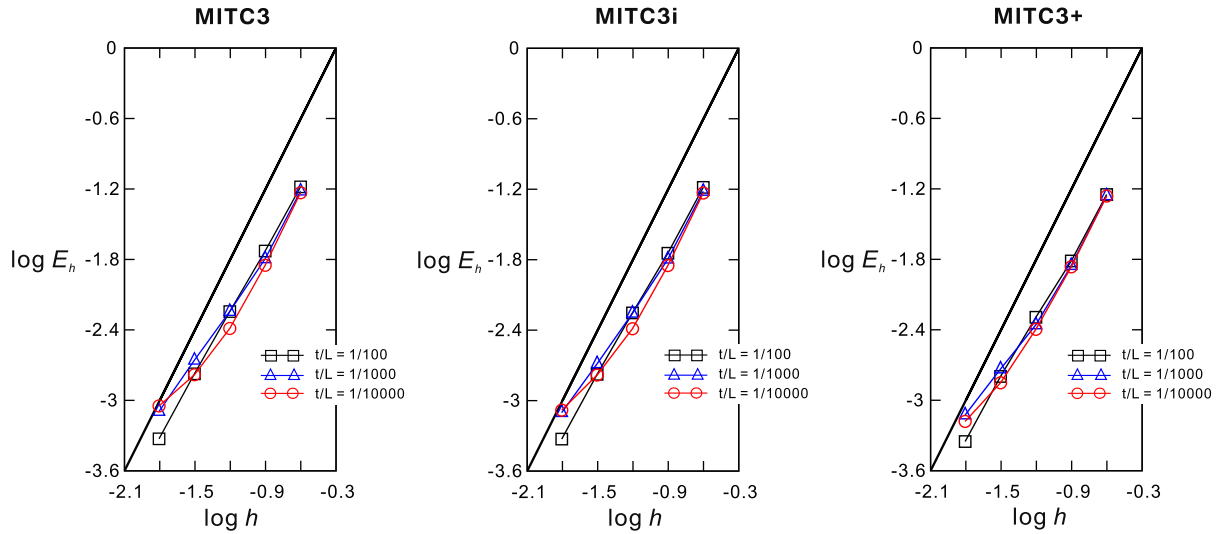


Fig. 13. Convergence curves for the free cylindrical shell problem. The bold line represents the optimal convergence rate.

4.2. Simply supported sixty-degree skew plate problem

Here we solve the sixty-degree skew plate bending problem shown in Fig. 9. The simply supported skew plate with its edges of length $2L$ and uniform thickness t is subjected to a uniform pressure. The boundary condition $u_z = 0$ is imposed along all edges [30].

The convergence behavior of the MITC3, MITC3i and MITC3+ shell elements is shown in Fig. 10. The reference solutions are obtained using a 128×128 element mesh of MITC9 shell elements. The solutions of the triangular shell elements are calculated using $N \times N$ element meshes ($N = 8, 16, 32, 64$ and 128). The element size is $h = 2L/N$. The performance of the MITC3+ shell element is much better than those of the other elements.

4.3. Cylindrical shell problems

We consider the cylindrical shell of length $2L$, radius R and uniform thickness t as shown in Fig. 11. The loading is a smoothly varying pressure $p(\theta)$

$$p(\theta) = p_0 \cos(2\theta). \quad (22)$$

This shell structure shows different asymptotic behaviors depending on the boundary conditions at its ends. When both ends are free, a bending dominated problem is solved, whereas when both ends are clamped, a membrane dominated problem is considered.

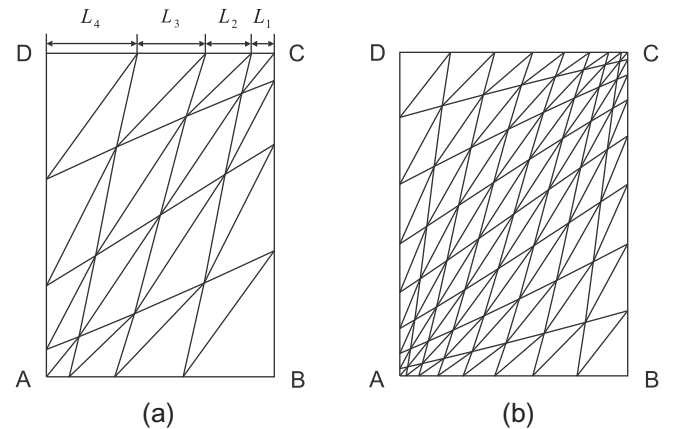


Fig. 14. Distorted mesh patterns (a) for $N = 4$ and (b) for $N = 8$.

Using symmetry, only the region ABCD in Fig. 11 is modeled. To have the membrane dominated problem, the clamped boundary condition is imposed: $u_x = \beta = 0$ along BC, $u_y = \alpha = 0$ along DC, $u_z = \alpha = 0$ along AB, and $u_x = u_y = u_z = \alpha = \beta = 0$ along AD. To have the bending dominated problem, the free boundary condition is imposed: $u_x = \beta = 0$ along BC, $u_y = \alpha = 0$ along DC, and $u_z = \alpha = 0$ along AB.

Figs. 12 and 13 give the convergence curves of the MITC3, MITC3i and MITC3+ shell elements for the clamped and free cylindrical shell problems. The reference solutions are calculated using a 96×96 element mesh of MITC9 shell elements. The solutions using the MITC3, MITC3i and MITC3+ shell elements are obtained with $N \times N$ element meshes ($N = 4, 8, 16, 32$, and 64). The element size is $h = L/N$. In these problem solutions, the MITC3, MITC3i and MITC3+ shell elements present similarly good convergence behaviors.

We then perform the convergence studies with the distorted meshes shown in Fig. 14. When a $N \times N$ element mesh is used, each edge is discretized in the following ratio: $L_1:L_2:L_3:\dots:L_N = 1:2:3:\dots:N$. Figs. 15 and 16 show the convergence curves

for the clamped and free cylindrical shell problems, respectively. The MITC3+ shell element shows an excellent performance.

4.4. Hyperboloid shell problems

Finally, we consider the hyperboloid shell shown in Fig. 17. The mid-surface of the shell structure is given by

$$x^2 + z^2 = 1 + y^2; \quad y \in [-1, 1]. \quad (23)$$

As for the cylindrical shell problems, a smoothly varying pressure is applied, see Fig. 11,

$$p(\theta) = p_0 \cos(2\theta). \quad (24)$$

A bending dominated behavior is obtained with free ends and a membrane dominated behavior is given with clamped ends. The bending dominated problem is known to be difficult to solve accurately [3].

Due to symmetry, the analyses are performed using one-eighth of the structure corresponding to the shaded region ABCD in

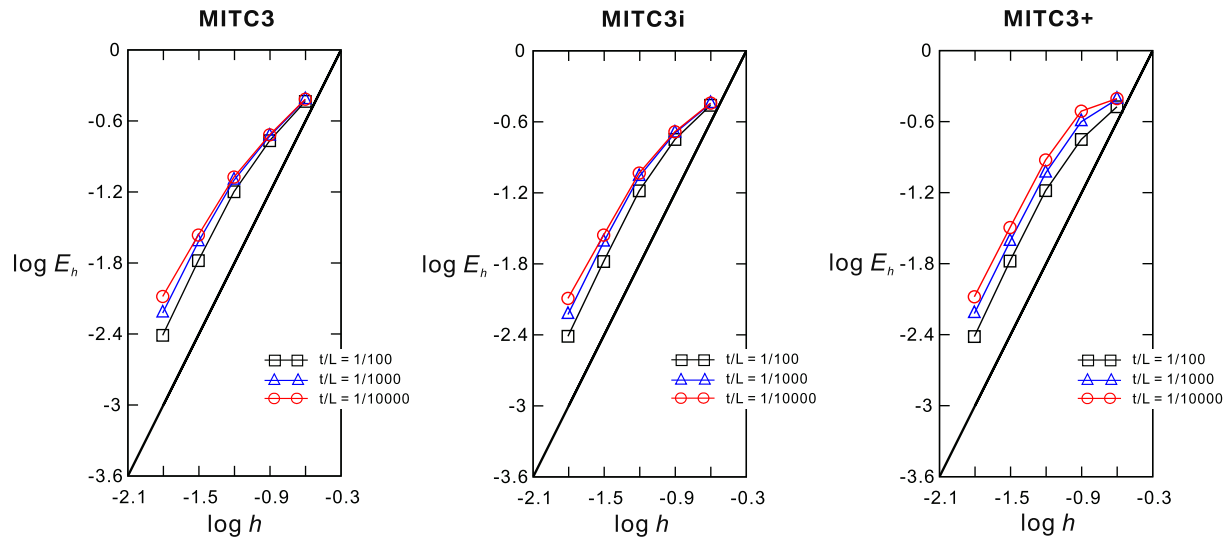


Fig. 15. Convergence curves for the clamped cylindrical shell problem with the distorted meshes shown in Fig. 14. The bold line represents the optimal convergence rate.

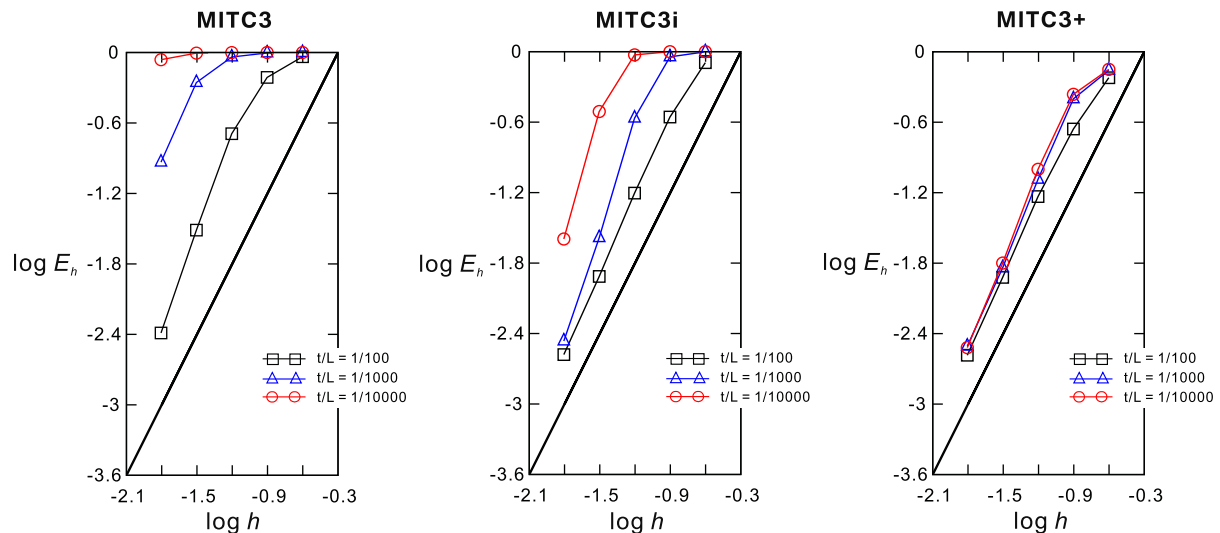


Fig. 16. Convergence curves for the free cylindrical shell problem with the distorted meshes shown in Fig. 14. The bold line represents the optimal convergence rate.

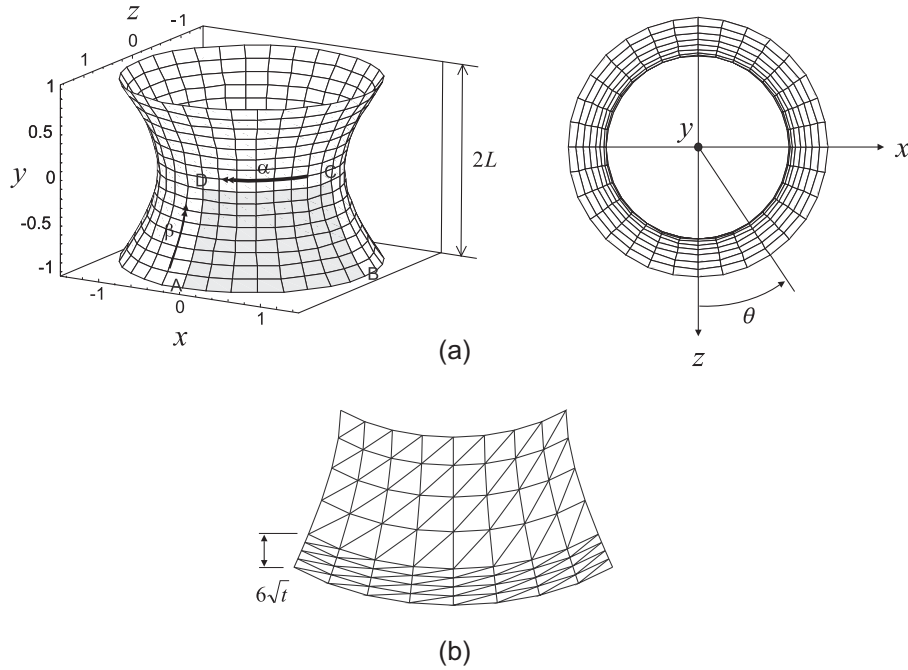


Fig. 17. Hyperboloid shell problem ($E = 2.0 \times 10^{11}$, $\nu = 1/3$ and $p_0 = 1.0$). (a) Problem description. (b) Graded mesh for the clamped case (8×8 mesh, $t/L = 1/1000$).

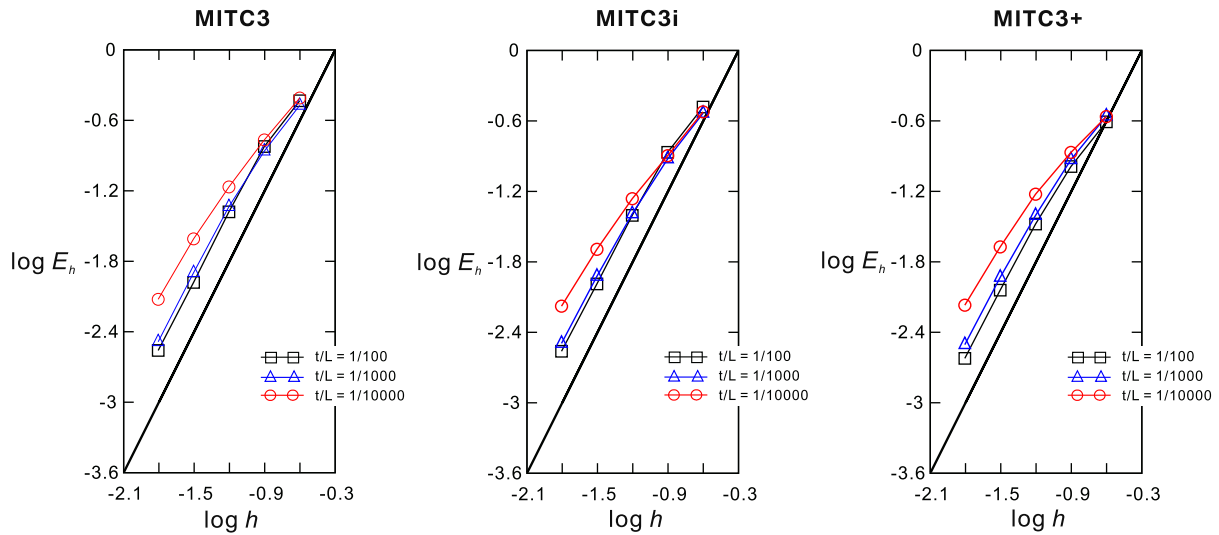


Fig. 18. Convergence curves for the clamped hyperboloid shell problem. The bold line represents the optimal convergence rate.

Fig. 17(a). For the membrane dominated case, the clamped boundary condition is imposed: $u_z = \beta = 0$ along BC, $u_x = \beta = 0$ along AD, and $u_y = \alpha = 0$ along DC, and $u_x = u_y = u_z = \alpha = \beta = 0$ along AB. For the bending dominated case, the free boundary condition is imposed: $u_z = \beta = 0$ along BC, $u_x = \beta = 0$ along AD, and $u_y = \alpha = 0$ along DC.

In both cases, a 96×96 element mesh of MITC9 shell elements is used to obtain the reference solutions. The solutions of the MITC3, MITC3i and MITC3+ shell elements are calculated using $N \times N$ element meshes ($N = 4, 8, 16, 32$ and 64). The element size is $h = L/N$. In the clamped hyperboloid shell case, a boundary layer of width $6\sqrt{t}$ is considered for half of the mesh, see Fig. 17(b). In the free hyperboloid shell case, the thin boundary layer is not specially considered [3].

Figs. 18 and 19 show the convergence curves for the clamped and free hyperboloid shell problems. In the clamped hyperboloid shell case, the performance of all three shell elements is similarly good. However, in the free hyperboloid shell case, the MITC3+ shell element shows a much better convergence behavior compared to the others.

Figs. 20 and 21 give the convergence curves of the MITC3, MITC3i and MITC3+ shell elements when the distorted meshes in Fig. 14 are used. The MITC3+ shell element displays even here an excellent convergence behavior.

We finally note that, in all the numerical studies in Sections 3 and 4, the standard 7-point Gauss integration is employed to calculate the stiffness matrix of the MITC3+ shell element [2]. If the standard 3-point Gauss integration is used for the MITC3+ shell

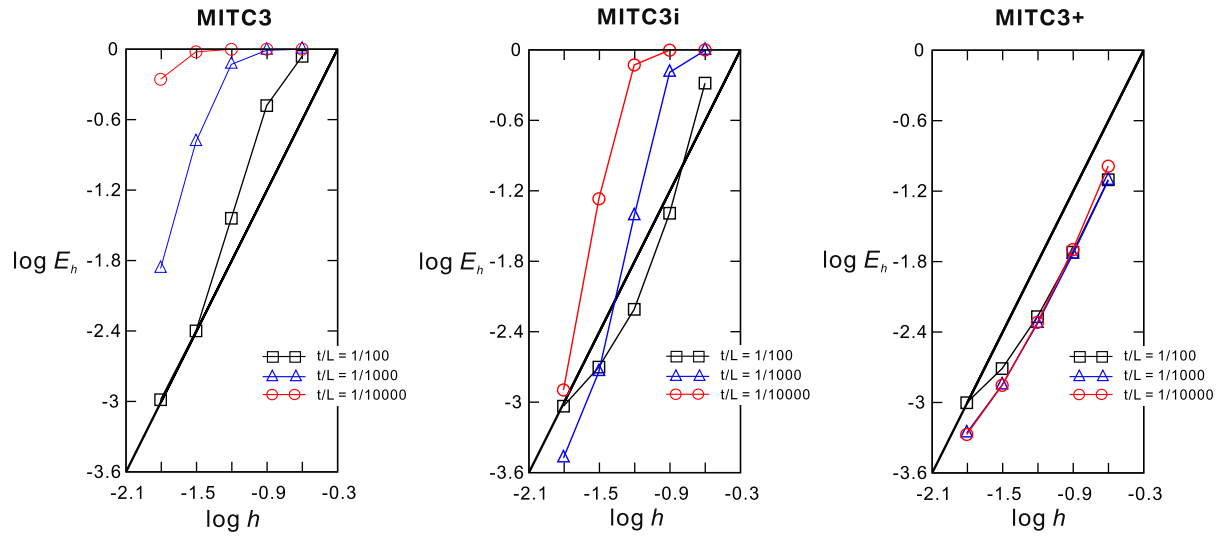


Fig. 19. Convergence curves for the free hyperboloid shell problem. The bold line represents the optimal convergence rate.

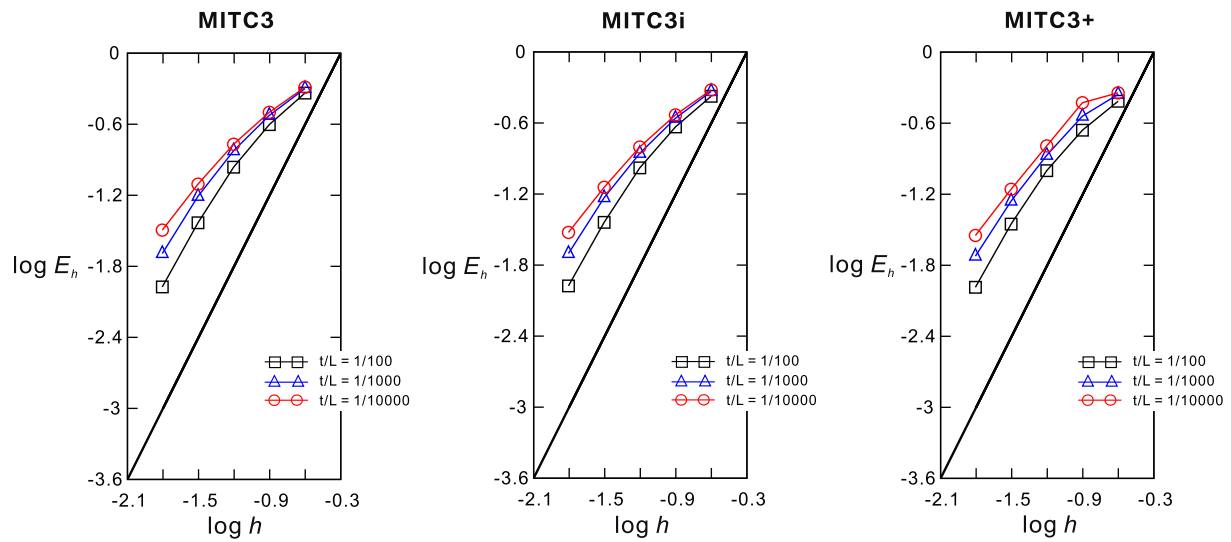


Fig. 20. Convergence curves for the clamped hyperboloid shell problem with the distorted meshes shown in Fig. 14. The bold line represents the optimal convergence rate.

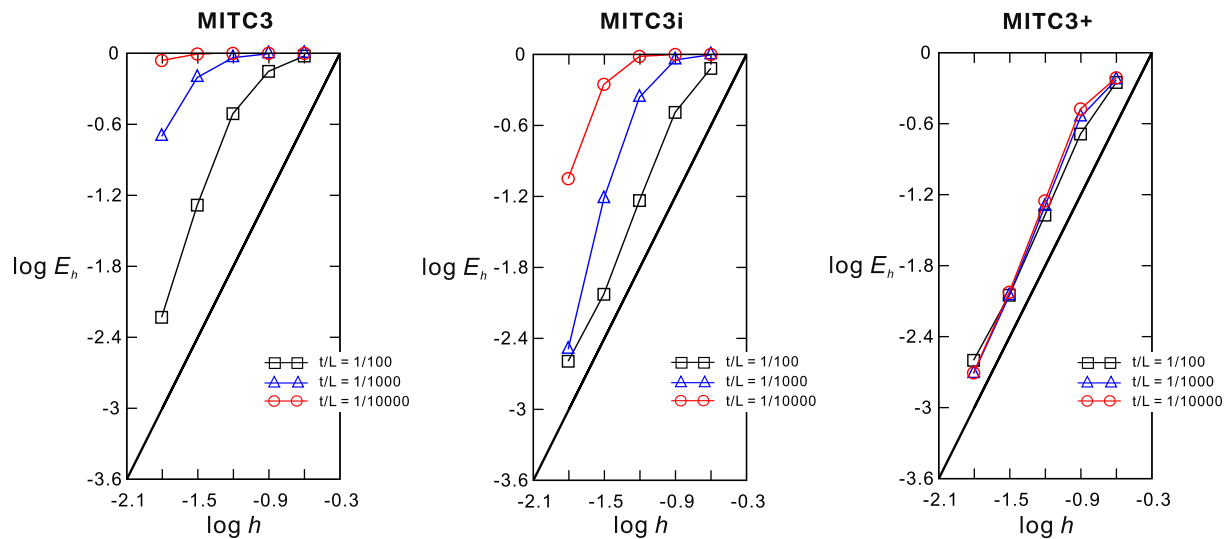


Fig. 21. Convergence curves for the free hyperboloid shell problem with the distorted meshes shown in Fig. 14. The bold line represents the optimal convergence rate.

element, all the basic numerical tests are also passed and similar convergence behaviors are observed.

5. Concluding remarks

In this study, we developed a new triangular shell element that shows considerable promise for general use. The MITC3+ element is based on the ‘basic mathematical shell model’ [3,35] and the MITC approach used for the development of triangular elements [1] but using a cubic bubble function for the rotations and a new assumed transverse shear strain field. For comparison, we also considered a shell element, in which the standard displacement interpolation of the 3-node shell element and the new assumed transverse shear strain field are used.

All shell elements considered pass the basic numerical tests, the isotropy, zero energy mode, and patch tests, and the MITC3+ shell element shows an excellent convergence behavior, even when using distorted element meshes. While only linear analysis conditions have been considered, the element formulation can directly be extended for large deformation analyses since only the usual MITC procedure has been used. In this paper, the effectiveness of the MITC3+ shell element was demonstrated only numerically, and a mathematical analysis would be very valuable to obtain further insight into the element behavior.

Acknowledgments

This work was supported by the Human Resources Development Program (No. 20134030200300) of the Korea Institute of Energy Technology Evaluation and Planning (KETEP) funded by the Ministry of Trade, Industry and Energy.

References

- [1] Lee PS, Bathe KJ. Development of MITC isotropic triangular shell finite elements. *Comput Struct* 2004;82:945–62.
- [2] Bathe KJ. *Finite element procedures*. New York: Prentice Hall; 1996.
- [3] Chapelle D, Bathe KJ. *The finite element analysis of shells – fundamentals*. 2nd ed. Berlin: Springer-Verlag; 2011.
- [4] Batoz JL, Bathe KJ, Ho LW. A study of three-node triangular plate bending elements. *Int J Numer Methods Eng* 1980;15:1771–812.
- [5] Felippa CA, Bergan PG. A triangular bending element based on an energy-orthogonal free formulation. *Comput Methods Appl Mech Eng* 1987;61:129–60.
- [6] Bletzinger KU, Bischoff M, Ramm E. A unified approach for shear-locking-free triangular and rectangular shell finite elements. *Comput Struct* 2000;75:321–34.
- [7] Argyris JH, Papadrakakis M, Apostolopoulou C, Koutsourelakis S. The TRIC shell element: theoretical and numerical investigation. *Comput Methods Appl Mech Eng* 2000;182:217–45.
- [8] Lee PS, Bathe KJ. Insight into finite element shell discretizations by use of the “basic shell mathematical model”. *Comput Struct* 2005;83:69–90.
- [9] Lee PS, Noh HC, Bathe KJ. Insight into 3-node triangular shell finite elements: the effects of element isotropy and mesh patterns. *Comput Struct* 2007;85:404–18.
- [10] Lee Y, Yoon K, Lee PS. Improving the MITC3 shell finite element by using the Hellinger–Reissner principle. *Comput Struct* 2012;110–111:93–106.
- [11] Bathe KJ, Lee PS. Measuring the convergence behavior of shell analysis schemes. *Comput Struct* 2011;89:285–301.
- [12] Chapelle D, Bathe KJ. Fundamental considerations for finite element analysis of shell structures. *Comput Struct* 1998;66:711–2, 19–36.
- [13] Baiocchi C, Lovadina C. A shell classification by interpolation. *Math Models Methods Appl Sci* 2002;12(10):1359–80.
- [14] Lee PS, Bathe KJ. On the asymptotic behavior of shell structures and the evaluation in finite element solutions. *Comput Struct* 2002;80:235–55.
- [15] Beirão da Veiga L. Asymptotic energy behavior of two classical intermediate benchmark shell problems. *Math Models Methods Appl Sci* 2003;13:1279–302.
- [16] Bathe KJ, Chapelle D, Lee PS. A shell problem ‘highly sensitive’ to thickness changes. *Int J Numer Methods Eng* 2003;57:1039–52.
- [17] Dvorkin EN, Bathe KJ. A continuum mechanics based four-node shell element for general nonlinear analysis. *Eng Comput* 1984;1:77–88.
- [18] Bathe KJ, Dvorkin EN. A formulation of general shell elements – the use of mixed interpolation of tensorial components. *Int J Numer Methods Eng* 1986;22:697–722.
- [19] Bucalem ML, Bathe KJ. Higher-order MITC general shell elements. *Int J Numer Methods Eng* 1993;36:3729–54.
- [20] Bathe KJ, Lee PS, Hiller JF. Towards improving the MITC9 shell element. *Comput Struct* 2003;81:477–89.
- [21] Kim DN, Bathe KJ. A triangular six-node shell element. *Comput Struct* 2009;87:1451–60.
- [22] Jeon HM, Lee PS, Bathe KJ. The MITC3 shell finite element enriched by interpolation covers. *Comput Struct* 2014;134:128–42.
- [23] Wilson EL, Ibrahimbegovic A. Use of incompatible displacement modes for the calculation of element stiffness or stresses. *Finite Elem Anal Des* 1990;7:229–41.
- [24] Arnold DN, Brezzi F, Fortin M. A stable finite element for the Stokes equations. *Estratto da Calcolo* 1984;21:337–44.
- [25] Kim J, Bathe KJ. The finite element method enriched by interpolation covers. *Comput Struct* 2013;116:35–46.
- [26] Kohno H, Bathe KJ. A flow-condition-based interpolation finite element procedure for triangular grids. *Int J Numer Methods Fluids* 2006;51:673–99.
- [27] Pinsky PM, Jasti RV. A mixed finite element formulation for Reissner–Mindlin plates based on the use of bubble functions. *Int J Numer Methods Eng* 1989;28:1667–702.
- [28] Hong WI, Kim YH, Lee SW. An assumed strain triangular solid element with bubble function displacements for analysis of plates and shells. *Int J Numer Methods Eng* 2001;52:455–69.
- [29] Ho SP, Yeh YL. The use of 2D enriched elements with bubble functions for finite element analysis. *Comput Struct* 2006;84:2081–91.
- [30] Lee PS, Bathe KJ. The quadratic MITC plate and MITC shell elements in plate bending. *Adv Eng Software* 2010;41:712–28.
- [31] Hiller JF, Bathe KJ. Measuring convergence of mixed finite element discretizations: an application to shell structures. *Comput Struct* 2003;81:639–54.
- [32] Bathe KJ, Iosilevich A, Chapelle D. An inf-sup test for shell finite elements. *Comput Struct* 2000;75:439–56.
- [33] Bathe KJ. The inf-sup condition and its evaluation for mixed finite element methods. *Comput Struct* 2001;79(243–52):971.
- [34] Bathe KJ, Brezzi F, Marini LD. The MITC9 shell element in plate bending: mathematical analysis of a simplified case. *Comput Mech* 2011;47:617–26.
- [35] Chapelle D, Bathe KJ. The mathematical shell model underlying general shell elements. *Int J Numer Methods Eng* 2000;48:289–313.